Photoelectrocatalytic degradation of refractory pollutants over WO₃/W network photoelectrode with heterophase junction for enhancing mass transportation and charge separation

Qiuling Ma [a], Rui Song [a], Fujun Ren [a], Hao Wang [a], Wensheng Gao [a], Zelong Li [a,*], Can Li [a,b,**]

[a] Key Laboratory of Advanced Catalysis, Gansu Province, State Key Laboratory of Applied Organic Chemistry, College of Chemistry and Chemical Engineering, Lanzhou University, Lanzhou, Gansu 730000, China

[b] State Key Laboratory of Catalysis, Dalian Institute of Chemical Physics, Chinese Academy of Sciences; Dalian National Laboratory for Clean Energy, Dalian, Liaoning 116023, China

ARTICLE INFO

ABSTRACT

The most crucial factors limiting the degradation performance of photoelectrocatalytic (PEC) process are the low charge separation efficiency and slow mass transportation. Herein, we report a WO₃ network photoelectrode by constructing heterophase junction of WO₃ on tungsten mesh (hm-m-WO₃/W mesh), which exhibits superior PEC performance, as high as 5.6 mA cm^{-2} of photocurrent density at 1.2 V$_{RHE}$, achieving a complete degradation (99.9%) and nearly total mineralization (84.5%) of bisphenol A, reaching an apparent reaction rate constant of 5.7×10^{-2} min^{-1}, 1.5 times of WO₃ based photoelectrode ever reported. A Schottky junction is formed at m-WO₃/W interface which greatly promotes the charge transfer between catalysts and support. The catalysts show appropriate phase alignment, where the parallel directions between built-in electric field of heterophase junction and external potential benefit charge separation. Computational fluid dynamics simulations indicate the network structure favors the diffusion of the fluid containing pollutants. This work demonstrates a viable strategy for designing the photoelectrode with high charge separation efficiency and fast mass transportation in PEC wastewater treatment.

1. Introduction

With the large-scale production of organic compounds in chemical industry, refractory organic pollutants with high stability and toxic matters have caused serious problems in almost all environmental matrices, which endangers the sustainable development of human beings [1–3]. Therefore, the degradation and mineralization of exposed refractory organic pollutants have become an urgent task. As an emerging wastewater treatment process, advanced oxidation processes (AOPs), has been implemented to degrade organic pollutants through the generation of reactive oxygen species (ROS), which enable the unselective and deep oxidation of a wide range of aqueous organic pollutants [4–6]. Among AOPs, PEC technology shows great potential in wastewater treatment because of the *in-situ* generation of ROS without adding any additional oxidants into the system and the lower financial costs in industrialization [7–10]. However, completely decomposing and mineralizing refractory organic pollutants by using PEC process with a high efficiency remains a grand challenge owing to their stable chemical structures [11–13].

PEC process with an external bias potential has been developed for diminishing electron-hole recombination and enhancing catalytic activity [14]. Nevertheless, the commonly used photoelectrodes usually encounter sluggish charge transfer and separation efficiency between catalyst and support electrode and hence leading to server charge recombination [15–17]. It is generally accepted that poor charge separation efficiency in catalysts restrains the PEC performance. Therefore, it is still necessary to pursue new strategies for achieving the efficient charge separation, such as morphology design [18,19], heterojunction fabrication [20–23], defective engineering [24,25] and surface modification [26,27]. The metal/semiconductor Schottky junction has

---

attracted considerable attention owing to its perfect role in improving the PEC performance, which can not only promote the charge transfer from catalyst to the metal electrode, but also form a Schottky barrier that is helpful for charge separation and transfer. A bilayer WO_3 n–n heterojunction constructed on tungsten foil with enhanced PEC performance was reported, and the good PEC performance originated from the efficient electron transport from catalysts toward the conductive tungsten foil [20]. For photocatalysts, the heterophase junction in polymorph semiconductors, such as TiO_2 and Ga_2O_3, can dramatically increase the PC activities for water splitting and pollutants degradation [28–30]. The unique function of a heterophase junction for charge separation and transfer has been well demonstrated. It is also found a composition of hexagonal/monoclinic WO_3 exhibits high separation efficiency of photoexcited electron-hole pairs, and the degradation performance of rhodamine B is significantly improved [31,32]. However, different from PC system, the key role of heterophase junction in PEC system is obscure because of exerting the bias potential. It has been reported that the poor PEC activity may be obtained that resulted from charge recombination at the ground boundaries of the particles without considering the alignment of different phases [28–30]. Therefore, a more rational design for the fabrication of phase junctions in a photoelectrode is highly necessary owing to the different charge transfer processes in various phase configurations [16]. Nevertheless, design and utilization of heterophere junction in WO_3 based photoelectrode in a PEC system for degradation of refractory pollutants have not been reported so far.

In addition, not like water splitting, the degradation of pollutants over most planar photoelectrochemical devices reported suffers from poor interfacial mass transportation and sluggish reaction kinetics. Thus, optimizations of the fluid diffusion and mass transportation of the pollutant in the PEC reactor is of importance [33,34]. The network electrode possesses flow-through architecture, which can make fluid diffuse uniformly and address the drawbacks of traditional planar photoanodes. In order to achieve a high degradation performance in a PEC system, developing new strategies for accelerating the fluid diffusion and fast transporting of reactants is also necessary.

Herein, WO_3 with a mixed phase structure grown on Tungsten (W) mesh was prepared to simultaneously improve the charge separation efficiency and mass transportation, and it can efficiently degrade and mineralize refractory organic pollutant, *e.g.*, bisphenol A (BPA) *via* a PEC process. The optimized photoelectrode with a mixed phase structure of WO_3 on the W mesh and both hexagonal and monoclinic WO_3 exposed on the surface of the photoelectrode (hm-m-WO_3/W mesh) exhibits the highest PEC performance in comparison with other mixed-phase samples. An impressive BPA degradation rate of 5.7×10^{-2} min^{-1} is achieved, which is two orders of magnitude higher than ever reported. The superior performance originates from the efficient charge separation and fast mass transportation. The obtained hm-m-WO_3/W mesh photoelectrode processes a Schottky barrier in the m-WO_3/W interface together with a rationally constructed phase junction structure, which greatly promotes the charge separation. Computational fluid dynamics simulations indicate that the W mesh supported network structure is in favor of the fluid diffusion and surface reactions of the pollutants in aqueous fluid. This work successfully demonstrates a new strategy for designing the photoelectrode with high charge separation efficiency and fast mass transportation in the photoelectrocatalytic wastewater treatment.

2. Experimental section

2.1. Preparation of the electrodes

The hexagonal-monoclinic phase junction WO_3/W mesh (hm-m-WO_3/W mesh) was prepared using a two-step hydrothermal method (Fig. S1). In detail, the synthesis of m-WO_3 was firstly conducted using a hydrothermal method reported by Shim Joo et al. [35] with some modification. Typically, 1 g of ammonium (para)tungstate hydrate was

added in 25 mL deionized water (DI water) and then 3.1 mL of HCl (3 mol L^{-1}) was drop wised into the solution with strong agitation for fully precipitating the H_2WO_4. After stirring for 1 h, the yellow gelatinous precipitate was formed. Subsequently, 2 mL of H_2O_2 was added with vigorously stirred for another 1 h with the transparent solution (peroxopolytungstic acid) was formed. Two pieces of W mesh (25×35 mm), which were previously washed with acetone, isopropyl alcohol (IPA), ethanol, and DI water in sequence, were leaned against the wall of a 50 mL Teflon-lined stainless-steel autoclave and the as-prepared precursor solution was filled into the reactor. The hydrothermal synthesis was carried out at 160 °C for 12 h. After reaction, the as-prepared samples were rinsed with DI water, dried, and further annealed at 500 °C for 2 h. The obtained electrodes were marked as m-WO_3/W mesh. Moreover, the samples annealed at 400 °C for 2 h were marked as h-WO_3/W mesh.

In order to obtain the hexagonal-monoclinic phase junction WO_3 (hm-m-WO_3), a mixed phase of hexagonal and monoclinic WO_3 (hm-WO_3) was constructed on m-WO_3 through the second-step hydrothermal treatment [36]. In detail, 0.5 g of ammonium (para)tungstate hydrate was added into 30 mL DI water. And 350 μL of concentrated HCl (36%–38%) dropped into the above solution with vigorously stirred for 0.5 h. Therefore, 1 mL of H_2O_2 and 0.25 g of citric acid were added into the gel with continuous stirring for 1 h to form precursor solution. Two pieces of as-prepared m-WO_3 were placed at the angle against the wall of the 50 mL Teflon-lined autoclave, and the precursor solution was filled into it. Subsequently, the sealed autoclave was heated at 160 °C for 12 h and was allowed to cool down naturally. The obtained electrodes were washed and calcined at 475 °C for 1 h, which was marked hm-m-WO_3. For controlling the loading amount of hexagonal phase, the hydrothermal time was adjusted from 5 h to 15 h during the synthesis.

2.2. Characterization

X ray diffraction (XRD) spectra was collected with a diffractometer (Rigaku D/Max-2400, Japan) and equipped with a Cu Ka radiation operating in a 2-theta range of 10–90° at a scan rate of 10° per minute. The morphologies and structures were characterized using scanning electron microscope (SEM, Thermo Scientific Apreo S, USA), high-resolution transmission electron microscope (HRTEM, FEI Talos F200s, USA) and high-resolution transmission electron microscopy (HRTEM, FEI Tecnai G2 Spirit Bio-TWIN, USA). Visible Raman spectra excited at 532 nm and 457 nm were acquired on a home-assembled Raman spectrograph (Renishaw in Via Raman microscope, UK) with a spectral resolution of 2 cm^{-1}. Ultraviolet photoelectron spectroscopy (UPS, Shimadzu Axis Supra, Japan) was conducted to obtain the work function of the samples. UV–visible diffuse reflectance spectra (UV–vis DRS) of all samples was measured on a UV–vis spectrophotometer (Shimadzu UV-3600, Japan) equipped with an integrating sphere while the absorption spectra were referenced to $BaSO_4$. Photoluminescence (PL) spectra were investigated using a Fluorescence Spectrofluorometer (Edinburgh Instruments FLS920, UK) and time-resolved photoluminescence (PL) spectra of the samples were also recorded with the excitation wavelength of 270 nm. Brunauer–Emmett–Teller (BET) surface area and corresponding textural properties were investigated from N_2 adsorption-desorption isotherms using BET analyzer (Micromeritics ASAP2460, USA).

2.3. Photoelectrochemical (PEC) measurements

Most of the photoelectrochemical (PEC) properties of the electrodes were evaluated with 0.1 M Na_2SO_4 aqueous solution (120 mL) in a three-electrode system controlled by the electrochemical workstation (Chenhua CHI760E, China), with the constructed WO_3/W mesh (working area of 25×30 mm) as the working electrode, pure graphene plate (30×50 mm) as the counter electrode and saturated calomel electrode (SCE) as the reference electrode, respectively. The light source was a

300 W Xenon lamp (Perfectlight PLS-SXE 300UVC, China). Linear sweep voltammetry (LSV) curves were acquired at scan rate of 50 mV s^{-1} and the photocurrent density of the photoelectrode was obtained by the photocurrent divide by the working area (7.5 cm^2). J-t curves were obtained through chronoamperometry (CA) with applied bias at 1.2 V$_{RHE}$. Mott-Schottky experiments were performed by using a setting frequency of 1000 Hz in the dark. Electrochemical impedance spectroscopy (EIS) was performed in a Princeton electrochemical workstation (PARSTAT MC 1000, USA) at 1.2 V$_{RHE}$ over the frequency range from 100 kHz to 0.01 Hz at an amplitude of 5 mV. The incident-photon-to-current conversion efficiencies (IPCE) was measured by a system (Feirea, China) operated with a monochromator, a 500 W Xenon lamp, a calibrated silicon photodetector, and a power meter. The charge injection efficiency is calculated according to the J-V curves measured in Na$_2$SO$_4$ (0.1 mol L^{-1}) and the mixture of Na$_2$SO$_4$ (0.1 mol L^{-1}) and H$_2$O$_2$ (0.5 mol L^{-1}). Calculated detailed shows as follows: the photocurrent of water splitting (J$_{H2O\ photocurrent}$) is a product of the rate of photon absorption expressed as a current density (J$_{absorbed}$), the charge separation yield of the photogenerated carriers (P$_{charge\ separation}$), and charge injection yield to the electrolyte (P$_{charge\ injection}$):

$$J_{H2O\ photocurrent} = J_{absorbed} \times P_{charge\ separation} \times P_{charge\ injection} \qquad (1)$$

The photocurrent measured in the electrolyte with H$_2$O$_2$ (J$_{H2O2\ photocurrent}$) is only a product of J$_{absorbed}$ and P$_{charge\ separation}$, assuming the charge injection yield becomes 100% (P$_{charge\ injection}$=1) in the presence of a hole scavenger (H$_2$O$_2$) in the electrolyte:

$$J_{H2O2\ photocurrent} = J_{absorbed} \times P_{charge\ separation} \qquad (2)$$

Based on Eqs. (1) and (2), the charge injection yield can be achieved:

$$P_{charge injection} = J_{H2O\ photocurrent} / J_{H2O2\ photocurrent} \qquad (3)$$

2.4. Computational fluid dynamics (CFD) simulations

The micro-flow and the fluid motion in the reactor were simulated by building two 3D geometries in the computational fluid dynamics (CFD) method. A CFD model is exhibited where the plate/network electrodes are placed in a rectangular channel. The size of grids in mesh electrode was set to 100 * 100 μm for consistent with the reality. Another CFD model simulated the fluid behaviors in the whole reactor with plate/network photoanodes, in which the whole calculation area is divided into a rotating domain and a stationary domain. In the rotating domain, the magneton rotation was simulated by means of a slip grid to introduce the rotational motion, and the motion transfer between domains was realized using an interface. In detail, the network photoanode was set as a porous media. The volume of fraction model (VOF) was used for the water-air two-phase and the RNG k-ε model was used for the turbulent motion, with a calculated time step of 0.001 s

2.5. PEC Degradation tests

BPA was selected as the target pollutant in the experiments. As seen from Fig. S2, the PEC degradation process was conducted in a quartz tubular reactor (150 mL) with a magnetic stirrer. It should be noted that the air atmosphere in the reactor was not swept before reaction, thus the electrolyte contained dissolved O$_2$ during the reaction with continuously stirring. A conventional three-electrode system was constructed using a CHI760E electrochemical workstation (Chenhua, China) coupled with a 300 W Xenon lamp (Perfectlight PLS-SXE 300UVC, China). The distance between the reactor and illumination source was 5 cm. Besides, the as-prepared electrode based on W mesh was served as the working electrode, a graphene plate (30 × 50 mm) and a saturated calomel electrode (SCE) were used as the counter electrode and the reference electrode, respectively. The electrolyte (120 mL) was consisted of BPA (20 ppm)

and Na$_2$SO$_4$ (0.1 mol L^{-1}). During the PEC process, a constant potential (1.2 V$_{RHE}$) was applied on the working electrode and a constant magnetic stirring rate of 300 rpm was kept. At certain intervals, 0.8 mL of the solution was withdrawn from the reactor and filtered by a 0.80 μm membrane filter for further analyzing. The direct photolysis of BPA, PC and EC processes were conducted by controlling the experimental conditions: in the absence of the catalyst, without applied bias, and without light illumination, respectively. For cyclic tests, the electrode was rinsed and dried for the next run. Typical radical scavenger of methanol (MeOH, 1 mol L^{-1}), EDTA-2Na (5 × 10^{-3} mol L^{-1}) or 4-Hydroxy-TEMPO (TEMPOL, 2 ×10^{-3} mol L^{-1}) was separately added into the system before reaction started in order to determine the contribution of the oxidative species generated during PEC degradation process. It should be noted that the concentration of all radical scavengers was over dosage in the system.

2.6. Analytical methods

Concentration of BPA was determined by high-performance liquid chromatography (HPLC, Agilent 1260 Infinity II, Germany) with a C$_{18}$ column (4.6 mm × 100 mm, 4 μm). The selected UV detection wavelength was 230 nm and the injection volume was 20 μL. A 30:70 (v/v) water/methanol mixture was used as the mobile phase at the flow rate of 1 mL min^{-1}. Total organic carbon (TOC) of the solution was investigated via a total organic carbon analyzer (Shimadzu TOC-L, Japan). Radical species were detected by electron paramagnetic resonance (EPR, Bruker A300–9.15/12, Germany) using DMPO as spin-trapping agents. During the detection of·O$_2$$^-$, the mixture solution of MeOH/Na$_2$SO$_4$ was used as the electrolyte to fully scavenge the·OH radicals since the signals of·OH may obstruct those of·O$_2$$^-$. 250 mg of DMPO was added into the PEC reactor (containing 30 mL electrolyte) before reaction started. During the PEC process, 1 mL of the solution was withdrawn and prepared for the EPR analysis. EPR spectra operating parameters were shown as follows: a center field of 3320 G, a sweep width of 100 G, a sweep time of 60 s, a modulation amplitude of 1 G, a modulation frequency of 100 kHz, a microwave frequency of 9.76 GHz and a microwave power of 20–30 mW at room temperature. Photoluminescence (PL) measurement was employed for the detection of •OH and TA with the initial concentration of 1.5 mmol L^{-1} served as a fluorescence probe molecule. The PEC process was carried out in a supporting electrolyte with TA dissolved in 0.5 mmol L^{-1}NaOH and 0.1 mol L^{-1} Na$_2$SO$_4$ aqueous solution. During the reaction, 2 mL of the reaction solution was taken out at certain intervals and measured on a FLS920 fluorescence spectrometer (Edinburgh Instruments, UK) with 315 nm excitation. Ultra-Performance Liquid Chromatography-Mass (UPLC-MS, Thermo Fisher Exactive plus) spectrometer fitted with electrospray ionization (EIS) source was used for mass analysis with a mass range from m/z 120–1000.

2.7. Calculation of energy consumption

Electric energy consumption (kWh g^{-1}) for BPA removal was calculated via the equation as follows:

$$EC = UIt/W \qquad (4)$$

where U denotes applied potential (V$_{RHE}$, V), I denotes measured current (A), t denotes reaction time (h), and W denotes weight of pollutant (BPA). Additionally, the electric energy consumption was correspondingly converted to US environmental price (US$). And the average electricity rate is 13.19 cents per kWh (May, 2021).

3. Results and discussion

3.1. Structural characterization

Fig. 1 illustrates the structure characterization of the WO$_3$ samples with different phase structures. The photographs of the photoelectrodes prepared are displayed in Fig. S3. The X-ray diffraction (XRD) pattern of hm-m-WO$_3$/W mesh (Fig. 1a) shows the mixed phases that include hexagonal and monoclinic WO$_3$ (JCPDS No. 75–2187 and No. 71–2141). The m-WO$_3$ prepared through the first-step hydrothermal process exhibits the typical monoclinic phase of WO$_3$ (JCPDS No. 71–2141), implying that the first-step hydrothermal process produces the monoclinic WO$_3$. The second-step hydrothermal process synthesizes both monoclinic and hexagonal WO$_3$ (Fig. S4). Raman spectroscopy is used to further confirm the phase structure of the WO$_3$ catalyst. Due to light absorption and light scattering, Raman spectroscopy with different laser sources can detect phases in different depths scattering intensity (I$\propto$(1/λ)^4). The laser sources at 457 nm and 532 nm in Raman spectroscopy can distinguish the phases from the outer layer to the bulk of the catalyst (Fig. 1b-c). As shown in Fig. 1b, Raman spectra excited by 532 nm laser, hm-m-WO$_3$ exhibits the same signals as m-WO$_3$ and these peaks match well with the monoclinic WO$_3$. However, Raman peaks of hm-m-WO$_3$ with a 457 nm laser (Fig. 1c) show six Raman bands, in which the peaks at around 270, 326, 714, and 809 cm^{-1}can be assigned to the monoclinic WO$_3$, and peaks at 251 and 690 cm^{-1} are corresponding to the hexagonal WO$_3$. It is suggested that the structure of hm-m-WO$_3$ contains both monoclinic and hexagonal phases and the hexagonal phase may be located in the outer region of the sample.

The scanning electron microscopy (SEM) images of hm-m-WO$_3$/W mesh photoanode show that the thick WO$_3$ films grown on the smooth-faced W mesh with a 3-D structure, and the average thickness of hm-m-WO$_3$ is 18.5 μm (Fig. 1d and Fig. S5). After synthesis, a network electrode with the grid size of *ca.* 125 * 125 μm^2 is obtained (Fig. S6). The SEM image of typical m-WO$_3$ that is prepared through the first-step hydrothermal process displays the nanoplate structure of monoclinic WO$_3$ and the thickness of nanoplates is measured to be around 9 μm (Fig. 1e and Fig. S5). After the second-step hydrothermal process, the nanoplates and hexagonal prisms are observed in hm-m-WO$_3$ (Fig. 1f), in which the hexagonal prisms corresponded to the hexagonal phase randomly distribute on the nanoplates. Fig. 1g shows intimate contact between monoclinic nanoplates and the hexagonal prisms, indicating the formation of the interface between two phases. High-resolution transmission electron microscopy (HRTEM) images of hm-m-WO$_3$ which are taken from the interface region show a clear phase boundary between monoclinic and hexagonal WO$_3$ (Fig. 1h and Fig. S7). The lattice spacing of 0.365 nm and 0.377 nm are corresponding to the (200) and (020) planes of the monoclinic WO$_3$, respectively, and the lattice spacing of 0.632 nm is consistent with the d value of the (010) and (100) planes of hexagonal WO$_3$. Additionally, the angle between the (020) and (200) planes of monoclinic WO$_3$ is measured to be 90°, while the (100) and (010) facets angle of 120° for hexagonal WO$_3$ is also observed, which is agreed well with the angle between the facets. The corresponded fast Fourier transform (FFT) patterns (Fig. 1i-j) exhibit a high crystalline nature with characteristic crystallographic orientations of (200), (220), and (020) for monoclinic WO$_3$, as well as (010) and (100) for hexagonal WO$_3$.

According to the above results, the preparation of the electrodes is schemed in Fig. 1k. The monoclinic WO$_3$ that contains nanoplate structures is loaded on the W mesh through the first-step hydrothermal process, and then the mixed phases of monoclinic and hexagonal WO$_3$ that show nanoplate and hexagonal prism structures have grown onto the electrode *via* the second-step hydrothermal process. The interface between monoclinic and hexagonal WO$_3$ was formed.

3.2. Photoelectric features

The photoelectric features of the WO$_3$ based electrodes are illustrated in Fig. 2. After *in situ* growing of WO$_3$ films on the W mesh, the migration of electrons from WO$_3$ to W mesh may be happened owing to different electron density of them. Thus, UV photoelectron spectroscopy (UPS) was employed firstly to determine the work functions of W mesh and m-WO$_3$ (Fig. 2a). The work functions of metallic W mesh and m-WO$_3$ are obtained as 5.32 eV and 4.82 eV, respectively. Using the calculated work function and Fermi level values, we created a band diagram of W/WO$_3$ interface to illustrate the Schottky junction (Fig. 2b). In this case, the charge transfer from catalysts to W support is improved, which is confirmed by the previous report. [20] Meanwhile, a Schottky barrier is formed to increase the resistance of electron transfer from W mesh to WO$_3$, which provides a driven force for directional movements of charges [37,38]. Therefore, electron can be easily transferred from WO$_3$ to W support and charge separation efficiency can be significantly improved.

The UV–visible diffuse reflectance spectra (UV–vis DRS) of h-WO$_3$, m-WO$_3$, and hm-m-WO$_3$ are shown in Fig. 2c. The prepared h-WO$_3$, m-WO$_3$, and hm-m-WO$_3$ show optical absorption edge at *ca.* 445, 425, and 426 nm, respectively. The optical bandgap of these samples can be determined by the Tauc formula (Fig. S8) and the calculated bandgaps of h-WO$_3$, m-WO$_3$ and hm-m-WO$_3$ are 2.72, 2.92, and 2.87 eV, respectively, which is in consistent with the WO$_3$ crystals reported in the database and reports [39,40].

Fig. 2d shows the Mott-Schottky plots generated from the capacitance values. The straight lines of all the samples display positive slopes, indicating the typical n-type semiconductor of the WO$_3$-based catalysts [41]. Compared with other WO$_3$ samples, the hm-m-WO$_3$ shows a much smaller slope. The carrier densities of h-WO$_3$, m-WO$_3$, and hm-m-WO$_3$ are calculated to be *ca.* 8.69×10^{20}, 4.98×10^{22} and 6.92×10^{23} cm^{-3}, respectively, according to the Mott-Schottky equation (Eq.5),

$$N_d=(2/e_0\varepsilon\varepsilon_0)[\mathrm{d}(1/C^2)/dV]^{-1} \tag{5}$$

where N_d is the carrier density (donor densities in this study), e_0 is the electron charge, ε is the dielectric constant of WO$_3$ (ε=20), ε_0 is the permittivity of vacuum and V is the applied potential. A higher N_d corresponds to a faster carrier transfer in the hm-m-WO$_3$ electrode, which results in an enhanced PEC performance. In addition, E$_{fb}$ values obtained from the *x*-axis intercept of h-WO$_3$, m-WO$_3$ and hm-m-WO$_3$ are *ca.* 0.38, 0.39, and 0.31 V$_{RHE}$ (inset of Fig. 2b), respectively, which represent the conduction band edge (E$_{CB}$) in the n-type semiconductor.

Combining with the results of UV–vis DRS and Mott-Schottky curves, the band structures of h-WO$_3$ and m-WO$_3$ are identified. As shown in Fig. 2e, the band structures of h-WO$_3$ and m-WO$_3$ match well and can feasibly form a charge separation path that is similar to type II heterojunction. Upon irradiation of WO$_3$ with formed heterophase junction, the photogenerated electrons transfer from the hexagonal phase to the monoclinic phase, while the photogenerated holes transfer from the monoclinic phase to the hexagonal phase. This phenomenon is interpreted by the potential difference in the band levels of two phases, namely the built-in electric field, which provides a driving force for efficient charge separation [28–30]. To further verify these results, the photochemical deposition experiments were carried out to study the charge separation behavior (Fig. S9) [42]. Selective depositions of Ag onto the monoclinic WO$_3$ and Co$_3$O$_4$ onto the hexagonal WO$_3$ respectively can be observed, which well evidences the separation and transfer paths of photogenerated electrons and holes induced by built-in electric field.

J-V curve of hm-m-WO$_3$/W mesh electrode exhibits a photocurrent density of *ca.* 5.6 mA cm^{-2} at 1.2 V$_{RHE}$, which is *ca.* 3.3 and 9.3 times of those obtained for the m-WO$_3$ (1.7 mA cm^{-2}) and h-WO$_3$ (0.6 mA cm^{-2}) electrode, respectively (Fig. 2f), and its photocurrent density is also superior to that of hm-WO$_3$ (3.2 mA cm^{-2}). The photocurrent density of
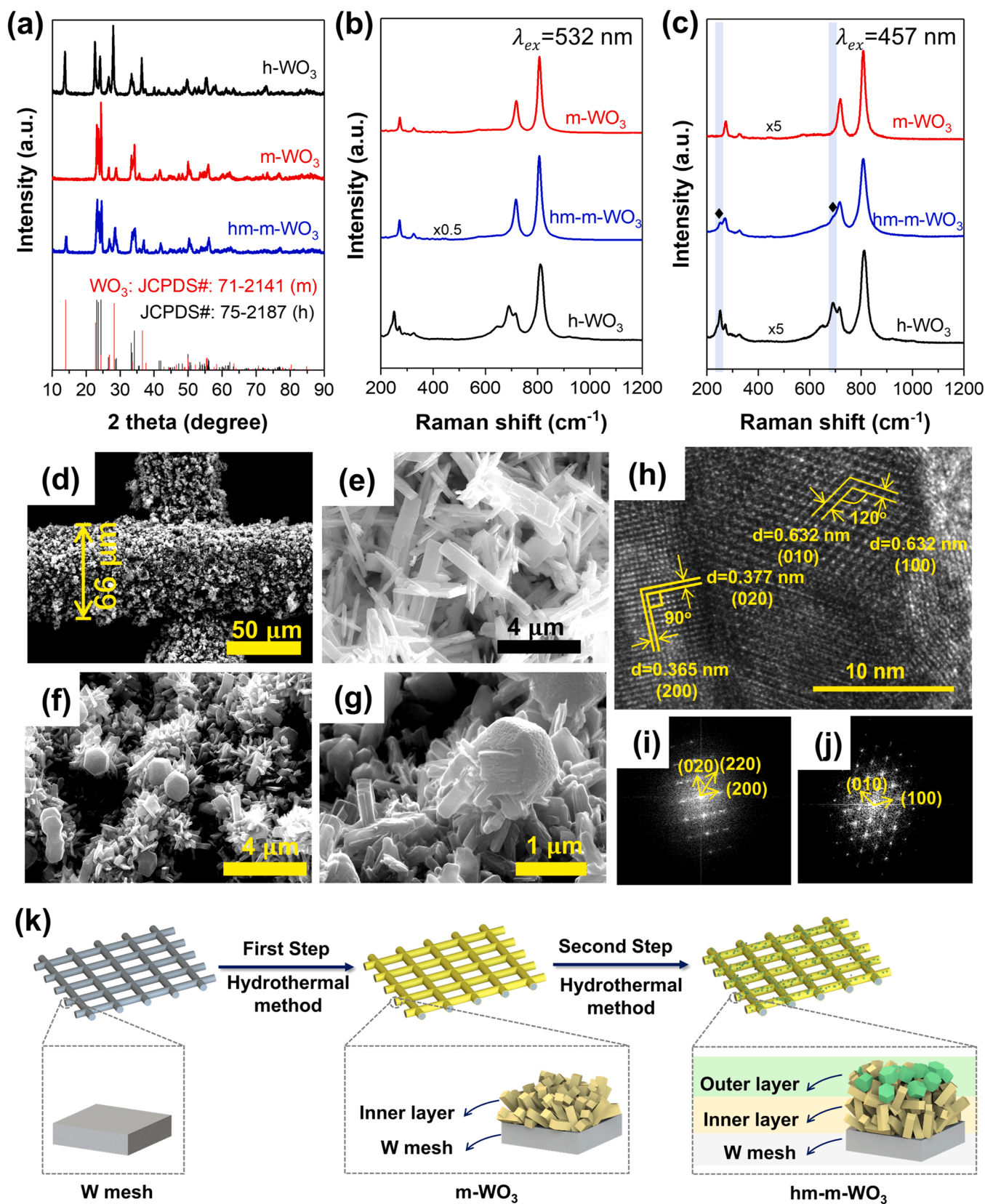
Fig. 1. (a) XRD patterns. (b) Raman spectra with 532-nm laser excitation. (c) Raman spectra with 457-nm laser excitation. (d) SEM image of hm-m-WO₃/W mesh electrode. (e) SEM image of m-WO₃. (f-g) SEM images of hm-m-WO₃. (h) HRTEM image of hm-m-WO₃. (i-j) The corresponding fast Fourier transform (FFT) patterns. (k) Illustration for the fabrication of hm-m-WO₃ on W mesh.
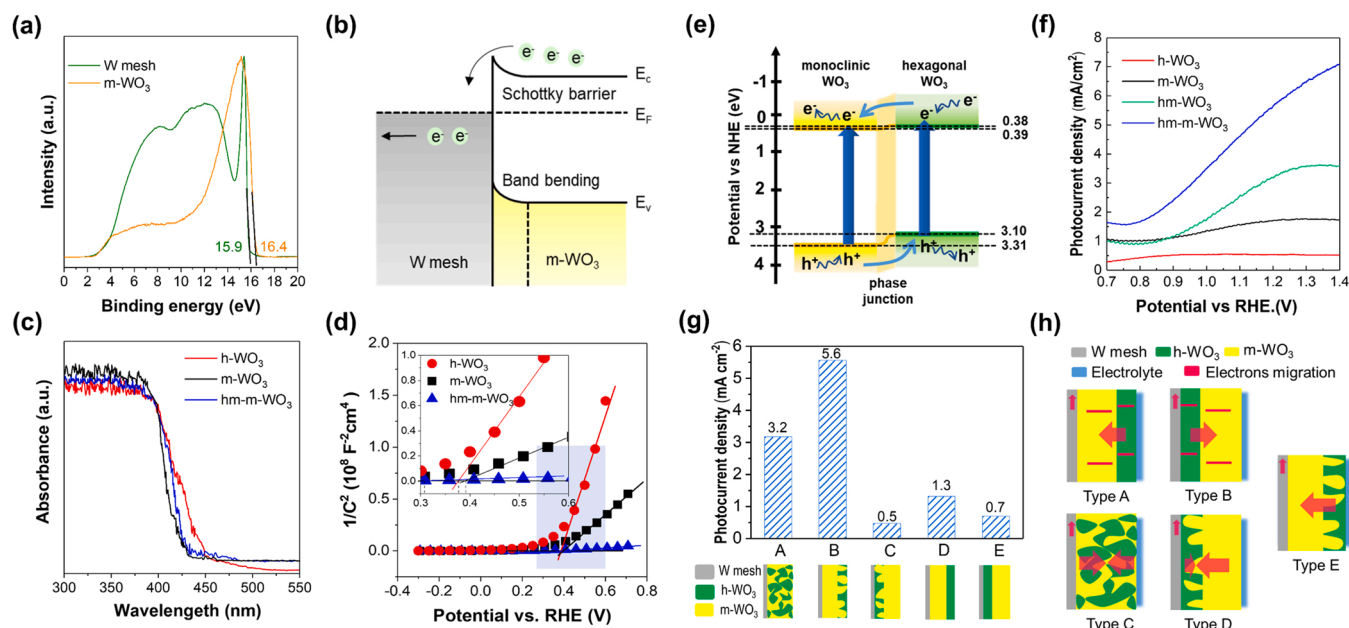
Fig. 2. (a) UPS spectra. (b) A schematic illustration of Schottky junction at W/WO$_3$ interface. (c) UV–vis DRS spectra. (d) Mott-Schottky plots. (e) Illustration of charge transfer across the heterophase junction. (f) J-V curves under light illumination. (g) Photocurrent density at 1.2 V$_{RHE}$ of different phase alignments of WO$_3$. (h) Schematic diagrams showing the phase effects on charge separation in PEC system.

WO$_3$ electrodes at 1.2 V$_{RHE}$ is in the order of hm-m-WO$_3$ >hm-WO$_3$ >m-WO$_3$ >h-WO$_3$. These results indicate that the phase structures and configurations significantly affect the photocurrent densities of the WO$_3$ electrode. Particularly, the WO$_3$ electrodes with heterophase junction show enhanced PEC performance. Thus, it suggests that the obvious enhancement of PEC activities in hm-m-WO$_3$ and hm-WO$_3$ is attributed to the heterophase junction formed in the catalysts. However, obvious differences between hm-m-WO$_3$ and hm-WO$_3$ in their PEC performances are also found.

To utilize the heterophase junction strategy in PEC system, the effects of phase configuration of WO$_3$ electrodes on the PEC performance were further investigated. Another three photoelectrodes with different phase configurations are constructed using a controllable two-step hydrothermal method (Named as y-x-WO$_3$, where x represents the inner layer, and y represents the outer layer). The structures of the three types electrodes were further confirmed by XRD and SEM (Fig. S10b-c). Therefore, there are totally five types of photoelectrodes with different phase configurations constructed (In detailed, A: h-m-WO$_3$, B: m-h-WO$_3$, C: hm-WO$_3$, D: m-hm-WO$_3$, and E: hm-m-WO$_3$). The photocurrent density of five types electrodes was obtained from their *J-V* curves at 1.2 V$_{RHE}$ (Fig. S10d and Fig. 2g), which follows the order: E > C> A> B> D. It is observed that the electrode with the monoclinic WO$_3$ phase directly contacted with W mesh shows the enhanced photocurrent densities in comparison with the electrode that the hexagonal WO$_3$ phase directly contacted with W mesh (E > D, A > B, E > C). Meanwhile, the WO$_3$ electrode with the heterophase junction on the outer layer (both monoclinic and hexagonal have been exposed on the surface of the electrode, E and C) can significantly enhance the photocurrent densities of the WO$_3$ electrode.

This phenomenon implies that the same direction of both the external circuit (E$_e$) and its built-in electric field (E$_i$) is a crucial factor for the highly efficient separation of the photogenerated electrons and holes in the PEC process. Fig. 2h schematically shows the effects of the different phase alignment on charge separation in PEC system. Since the direction of E$_i$ is from hexagonal to monoclinic phase, the WO$_3$ electrode in Type B or Type D shows the reverse direction of E$_i$ and E$_e$, which results in a low PEC activity. It indicates that hexagonal phase WO$_3$ located in inner layer of the photoelectrode can unexpectedly lead to

charge recombination during the PEC process owing to the reversed band structure configuration. In the Type C, the vector direction of E$_i$ is uncertain due to random phase junction, and it shows moderate PEC activity. Thus, to boost a PEC reaction, the structure of the phase junction should not be disordered as it can also serve as charge recombination centers. The phase alignments in Type A and Type E are suggested to be obtained in the WO$_3$ based system owing to the same vector directions between E$_i$ and E$_e$ [28–30]. In this situation, the driving force provided by the built-in electric field at the interface of the hexagonal-monoclinic WO$_3$ phase junction enhances the separation of charges, which significantly improves the PEC performance.

Moreover, the interfacial structure between two phases is vitally important in a PEC system as well. As seen from Fig. 2e, the samples that both monoclinic and hexagonal have been exposed on the surface of the electrode (Type E and Type C) show improved photocurrent densities in comparison with Type A. According to the SEM results (Fig. S10c), tightly interfacial contact between two phases is found in Type E and Type C electrodes, which therefore promotes the charge separation efficiency. However, the surface of Type A sample is fully covered by hexagonal WO$_3$ without interfacial structures, which is much similar to h-WO$_3$. On the basis of these results, it is demonstrated that the interfacial structure between two phases is decisive for the efficient charge separation. The above results explain why Type E (hm-m-WO$_3$) shows highest PEC activity.

3.3. Charge separation and transfer dynamics

To further understand the origins of the outstanding PEC performance of the hm-m-WO$_3$/W mesh catalyst, the separation and transfer dynamics of photogenerated charge carriers were investigated. Fig. 3a displays the electrochemical impedance spectra (EIS) with/without light illumination. The EIS plots of the WO$_3$ based photoanodes in dark present semicircles, indicating that the surface catalytic oxidation processes are mainly controlled by the electrochemical reaction. When the light on, the arc radiuses of the samples significantly decrease, implying a remarkable increase of the electron mobility. The hm-m-WO$_3$/W mesh with light illumination exhibits the smallest arc radius of the EIS plots among the WO$_3$ electrode, which suggests the fastest charge transfer
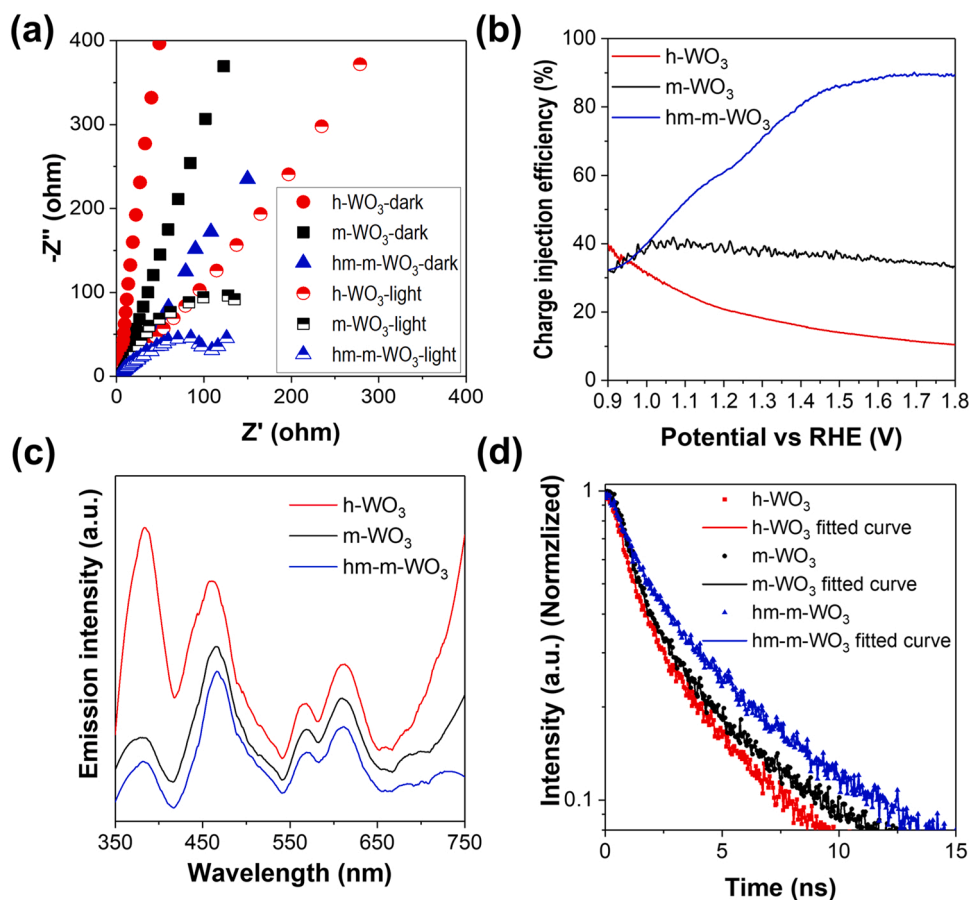
Fig. 3. (a) EIS plots with or without light illumination. (b) Charge injection efficiency *versus* potential curves. (c) PL spectra. (d) Time-resolved PL spectra.

kinetics and the most efficient separation of the photogenerated electrons and holes among the electrodes. These results further verify that the heterophase junction introduced in WO₃ based photoelectrode promotes the charge separation.

We therefore examined charge injection efficiencies of the h-WO₃/W mesh, m-WO₃/W mesh, and hm-m-WO₃/W mesh electrodes by comparing the photocurrent from the oxidation of water and H_2O_2 [43]. As seen from Fig. 3b, the charge injection efficiencies of h-WO₃/W mesh and m-WO₃/W mesh are rather poor, indicating that photogenerated holes are accumulated on the surface [44]. Those decreased charge injection efficiencies at the high potential region are attributed to the kinetic bottleneck [45]. Once constructing heterophase junction, the charge injection efficiency of hm-m-WO₃ is substantially enhanced, reaching *ca.* 60% at a potential of 1.2 V_{RHE}, suggesting that around 60% of the interfacial holes (*i.e.*, photogenerated and separated) are utilized for surface reaction. It is clear that the heterophase junction as the build-in electric field provides the driven force for charge separation, thus the surface recombination is inhibited. The incident-photon-to-current conversion efficiencies (IPCE) were measured (Fig. S11) as well. The hm-m-WO₃/W mesh reveals higher IPCE values compared with h-WO₃/W mesh and m-WO₃/W mesh, and an IPCE value of *ca.* 66.2% is obtained for the hm-m-WO₃/W mesh at 350 nm.

Fig. 3c displays the photoluminescence (PL) spectra of the catalysts with the excitation wavelength of 254 nm. The PL intensity of hm-m-WO₃ dramatically decreases in comparison with h-WO₃ and m-WO₃, indicating the reduced amount of carrier recombination.

In order to understand the charge transfer dynamics of the WO₃ catalysts, Time-resolved PL spectra were conducted (Fig. 3d). As seen, the hm-m-WO₃ with mixed phases exhibits slightly slower fluorescent decay kinetics than that of h-WO₃ or m-WO₃. The Time-resolved PL

spectra can be fitted into the triple exponential decay function, and the average lifetime of h-WO₃, m-WO₃, and hm-m-WO₃ is calculated to be 5.80, 5.96, and 6.21 ns, respectively (Table S1). Owing to the effective spatial charge separation by the heterophase junction in WO₃, the hm-m-WO₃ shows the longest average decay lifetime, indicating more photogenerated charges can participate in the reaction, which is beneficial for improving the PEC performance.

3.4. Fluid behaviors

In consideration of poor interfacial mass transportation and sluggish reaction kinetics as a bottleneck of plate photoelectrochemical devices for efficiently degrading pollutants, a network electrode is employed to optimize the fluid diffusion around the surface of the electrode and in the whole system. Fig. 4a shows the scheme of the hm-m-WO₃/W mesh electrode as a network electrode with flow-through architecture developed to improve the pollutant containing fluid diffusion and accelerate the transportation of reactants by making the fluid flow through the grids. The computational fluid dynamics (CFD) simulations were carried out to understand the fluid behaviors difference between plate and network electrode [46]. Fig. 4b-c displays the velocity contours of plate and network electrode which is placed in a flowing liquid (CFD Model was displayed in Fig. S12). It can be observed that the fluid behavior in mesh electrode is very different from the plate electrode (Fig. 4b). The grids in mesh electrodes are used as the flow-fluid channels for facilitating the transportation of microfluidic in interspace, which is beneficial to the contact between pollutant and catalysts. In contrast, plate electrode completely blocks the liquid flowing. Seen from the side view (Fig. 4c), the liquid flows through the top and bottom sides of plate electrode and thereby causes a low-velocity area near the surface of electrode, which is unfavorable for the efficient contact between the
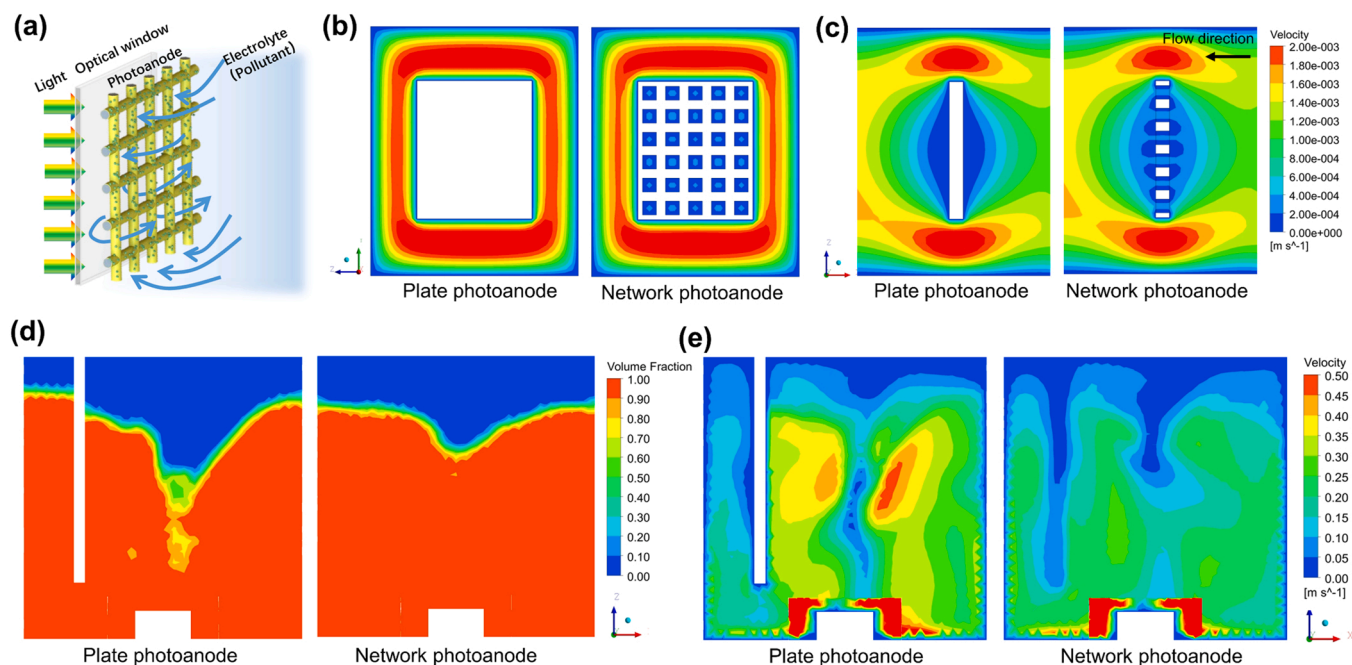
Fig. 4. (a) Schematic drawing of fluid behaviours around the network photoanode. (b-c) CFD simulations of the flow velocity in plate or network electrode in a flowing water ((b) is the front view, and (c) is the side view). (d-e) CFD simulations of the fluid behaviours of the whole system with plate or network photoanode ((d) volume fraction distribution, and (e) velocity distribution).
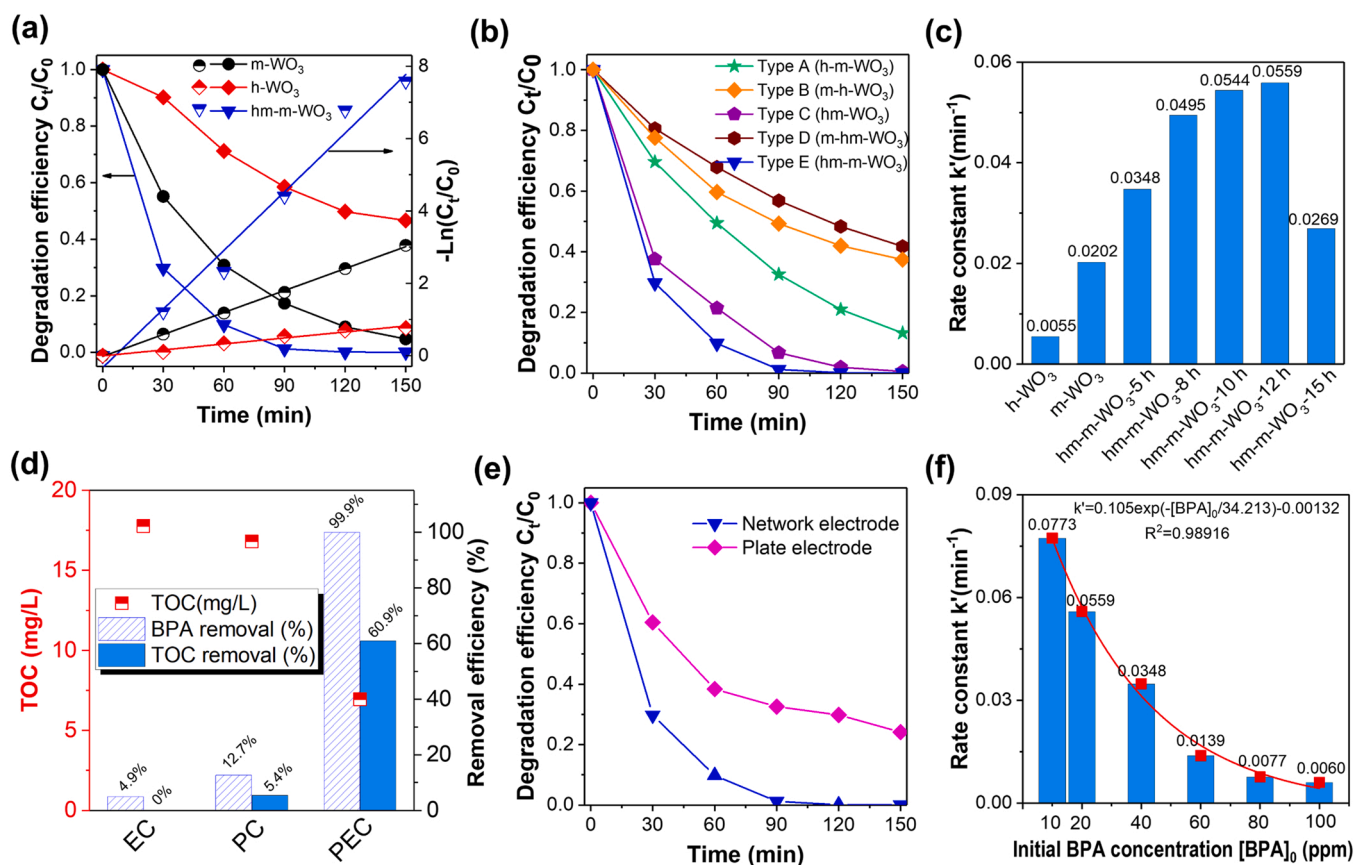

Fig. 5. (a) PEC degradation and first-order reaction kinetics of BPA removal. (b) PEC degradation by different phase alignments of WO₃. (c) The reaction rate in hm-m-WO₃/W mesh with different hydrothermal time. (d) Degradation of BPA by hm-m-WO₃/W mesh *via* EC, PC, and PEC processes. (e) PEC degradation by network and plate electrodes. (f) The reaction rate in various initial BPA concertation.

pollutant with low concentration and catalysts. It is interesting that more liquid flows through the network electrode, which significantly reduces the low-velocity area on the surface of electrode and enhances the contact probability between pollutant and catalysts.

The fluid behaviors of the whole system with plate/network photo-anode were also investigated with the CFD simulations (CFD Model was displayed in Fig. S13). The volume fraction contours of plate and network photoanodes (Fig. 4d) displays the decreases of the center liquid level in both plate and network photoanodes because the rotational flow driven by the rotor at the bottom causes a reduction of pressure. However, a partition of liquid level can be found on the sides of plate photoanode, indicating the plate obviously hinders the fluid flowing in the system, especially the liquid between the photoanode and light window. The liquid level in the whole system with network electrode is continuous, which implies the mesh electrode makes the pollutant containing fluid diffusion more uniform. The velocity distributions in these two systems also exhibit obvious differences (Fig. 4e). In the plate photoanode/system, the fluid velocity in the left side of the plate is much lower than the right side, demonstrating the fluid between electrode and light window cannot efficiently diffuse into the whole system. In contrast, a uniform fluid velocity distribution is observed in the system with a mesh photoanode. Therefore, the fluid flows rotationally in the whole system when using a network photoanode, which enables the rapid diffusion of reactants and enhances the contact probability between organic matters and catalysts, resulting in the improvement in mass transportation of pollutants.

3.5. PEC degradation performance

PEC degradation of BPA, a recalcitrant organic pollutant, was investigated as the probe reaction to evaluate the PEC performance of the as-prepared WO$_3$ photoanodes. The BPA removal kinetics was fitted by the first-order reaction using Eq. 6, where k' is a pseudo-first-order rate constant.

$$(d\,[BPA])/dt = -k'[BPA] \tag{6}$$

Fig. 5a displays the BPA degradation activities of h-WO$_3$/W mesh, m-WO$_3$/W mesh, and hm-m-WO$_3$/W mesh photoanodes *via* PEC process. The h-WO$_3$ and m-WO$_3$ grown on W mesh exhibit respectively 53.4% and 95.3% of BPA removal efficiencies, and the TOC removal efficiencies of h-WO$_3$ and m-WO$_3$ show less than 25% for 150 min reaction (Fig. S14). Notably, the hm-m-WO$_3$/W mesh shows significantly increased in PEC degradation efficiency. The BPA is nearly total degraded in only 90 min with the TOC removal efficiency of 60.9% within 150 min, which corresponds to its superior PEC performance and uniform fluid distribution in the whole system. BPA is relatively stable under light illumination with only 9.7% removal obtained in photolysis (Fig. S15). Pure W mesh as the support of the electrode exhibits low PEC activity and only 15.5% BPA is removed (Fig. S16). The hm-m-WO$_3$ electrode with a low surface area ($<1\,m^2\,g^{-1}$) shows the poor ability for BPA adsorption (Fig. S17–18). Thus, the significant enhancement in BPA degradation is mainly attributed to the intrinsic PEC activity of the catalyst. The intrinsic activity of h-WO$_3$, m-WO$_3$, or hm-m-WO$_3$ is investigated by normalizing the apparent kinetic constant of PEC degradation of BPA using the surface area (the results showed in Fig. S19). The normalized rate constant of hm-m-WO$_3$ is *ca.* 5.7×10^{-2} min^{-1}, which is *ca.* 7.5 and *ca.* 2.3 times those of h-WO$_3$ and m-WO$_3$, respectively. Additionally, the PEC activity by normalizing the apparent kinetic constant using the loading mass of catalysts is carried out with results shown in Fig. S20, which indicates that the normalized rate constant of hm-m-WO$_3$/W mesh is *ca.* 5.35 min^{-1} g^{-1}, which is *ca.* 6.1 and *ca.* 2.2 times those of h-WO$_3$ and m-WO$_3$, respectively, confirming the significance of heterophase junction in improving the PEC degradation performance.

Different phase configuration of WO$_3$ electrodes on degradation of BPA *via* PEC process are further investigated with results displayed in Fig. 5b and Fig. S21. The PEC degradation efficiency and TOC removal efficiency follow the order of: E > C > A > B > D, which keeps in accordance with the order of photocurrents. When utilizing the heterophase junction in WO$_3$ based electrodes, the structure where monoclinic WO$_3$ is located in the bulk and both hexagonal and monoclinic WO$_3$ are exposed on the surface of the photoelectrode shows superior PEC degradation activity of BPA, which is suggested to be fabricated. Above results evidence the importance of phase alignment in improving PEC performance, and strongly support our claim that the improvement of the PEC performance of hm-m-WO$_3$ photoelectrode is unambiguously duo to the well-defined monoclinic-hexagonal heterophase junction.

The mixed phases formed in the second-step hydrothermal process has crucial impacts on PEC activity. Changing the hydrothermal time in the second step influences the loading content of the hm-WO$_3$ without affecting the phase structures (Fig. S22). The optimized hm-m-WO$_3$ with a hydrothermal time of 12 h shows the highest PEC degradation rate constant of 5.6×10^{-2} min^{-1} (Fig. 5c). Fig. S23 displays the overall PEC degradation performances, where nearly total degradation of BPA is achieved by hm-m-WO$_3$/W mesh with various hydrothermal times. Besides, the TOC removal efficiency increases by prolonging the hydrothermal time from 5 h to 12 h, while decreases with further increasing the hydrothermal time to 15 h. Varying of the hydrothermal time results in the different interfacial areas between hexagonal and monoclinic phases, which can affect the formation of the built-in electric field. These results indicate the improved degradation efficiency indeed originates from the tunable built-in electric field but not from the increasing the content of hexagonal WO$_3$.

Comparative experiments in PC and EC conditions were also carried out to evaluate the PEC activity of hm-m-WO$_3$/W mesh. The PC and EC show the lower activity in removing the BPA (Fig. 5d). The apparent kinetic constant of BPA removal by PC, EC, and PEC is 2.5×10^{-4}, 8.2×10^{-4}, and 5.4×10^{-2} min^{-1}, respectively. It indicates that PEC, the combination of PC with EC makes the BPA degradation and mineralization much more efficient, implying a significant synergetic effect between the photo and electric energy. Aiming to explore the synergistic effect of PC and EC, the PEC degradation processes were conducted under specific incident light with different wavelengths or various applied voltages subsequently (Fig. S24–25). It can be obtained from the results that the PEC performance in various light wavelengths is interrelated to the light absorption properties of hm-m-WO$_3$/W mesh. And the main role of applied bias is to provide a driven force for the separation and directional migration of photogenerated charges. Above results demonstrate that in the PEC system, photogenerated electron-hole pairs are effectively separated and the photogenerated electrons are extracted to the outer circuit by applying the bias across the WO$_3$ film, leading to an enhanced separation of photogenerated charges.

The impact of network electrode on the mass transportation of pollutants was therefore deliberated by comparing its PEC degradation performances with plate electrode. As illustrated in Fig. 5e, 99.9% and 75.8% of BPA are decomposed within 150 min by network and plate electrodes, respectively. Moreover, the network electrode with a flow-through mode shows a rate constant of 5.4×10^{-2} min^{-1}, which is 6.1 times higher than that of plate electrode (8.9×10^{-3} min^{-1}). It is because the contaminated water can flow through the mesh of the network electrode, enhancing rates of mass transportation around the surface of the electrode and the whole system, which also verifies the CFD simulation results.

In order to further investigate the degradation kinetics, effects of initial BPA concentration on degradation rate constant in hm-m-WO$_3$/PEC system are conducted (Fig. 5f and Fig. S26). A continuous decreasing of k' is observed with the increment of [BPA]$_0$ from 10 to 100 ppm, which is described by an exponentially decreasing function (k'=0.105exp(-[BPA]$_0$/34.213)− 0.00132), and the TOC removal efficiency also exhibits a declining tendency. It is inferred that the PEC degradation of BPA on the electrode surface depends on both the surface

oxidation kinetics and mass transportation kinetics. With the high initial concentration of BPA, the generated oxidative species in the PEC system may be exhausted by an overdose of BPA, leading to the sluggish kinetics of BPA degradation. Although the degradation and mineralization efficiencies of BPA show declining tendencies when increasing initial BPA concentration, the total removal amounts of BPA and TOC are largely increased. From the result, it can be inferred that the network electrode has improved the pollutant containing fluid diffusion and mass transportation across the electrode and in the whole system, which is beneficial for the PEC degradation and mineralization at the high initial

concentration of BPA.

It is worthwhile mentioning that hm-m-WO₃/W mesh shows superior degradation efficiency of refractory pollutant, which is an impressive catalytic performance among the reported catalyst photoanodes for PEC degradation of BPA and WO₃-based photoanodes in PEC degradation applications (Table S2).

3.6. Mechanism in PEC degradation process

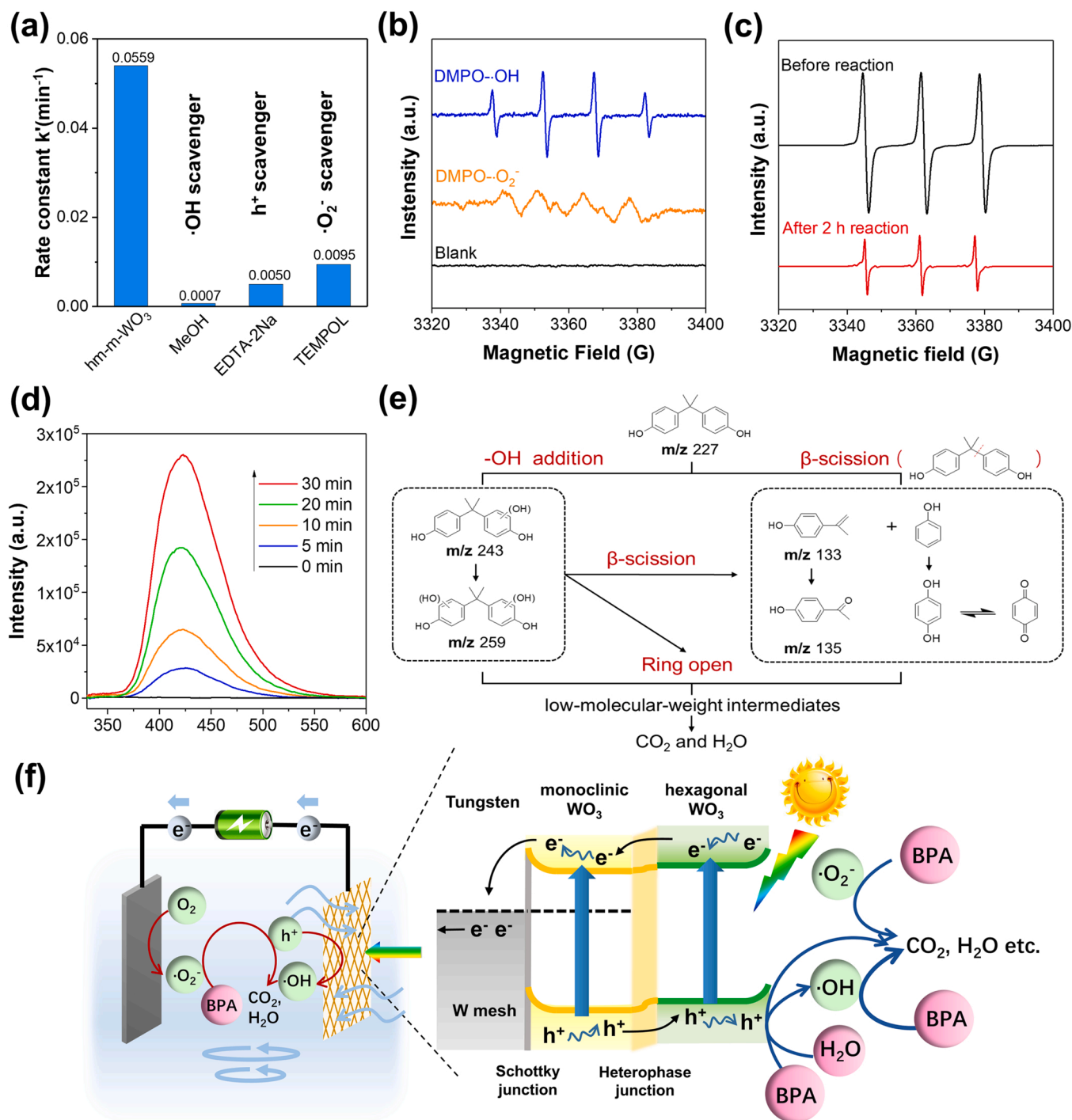The PEC degradation of organic pollutants has been mainly ascribed

Fig. 6. (a) Comparison of reaction rate under different quenching conditions. (b) EPR spectra with DMPO added in the PEC process. (d) EPR spectra with TEMPOL added in the PEC process. (d) PL spectra in the solution of terephthalic acid. (e) Possible BPA degradation pathways. (f) Schematic mechanism of PEC degradation performance by hm-m-WO₃/W mesh.

to the oxidation reaction of the ROS such as •OH and •O_2^- as well as the oxidative holes (h^+) [47]. To reveal the underlying degradation mechanism, radical scavengers (methanol (MeOH) for •OH, 4-Hydroxy--TEMPO (TEMPOL) for •O_2^- and EDTA-2Na for h^+) were separately added into the reaction system under typical reaction conditions [48]. The inhibiting effects of three scavengers are obvious, indicating that •OH, •O_2^- and h^+ collectively play important roles in the PEC degradation process (Fig. 6a). The BPA removal efficiencies are 10.0% for MeOH, 76.7% for TEMPOL and 54.1% for EDTA-2Na (Fig. S27). In comparison with the blank experiment, the contribution of ROS for BPA degradation by hm-m-WO_3 follows the order: •OH >h^+>•O_2^- and •OH is the dominant oxidative species. However, the orders of ROS contribution in h-WO_3/PEC and m-WO_3/PEC systems are similar as follows: •O_2^->•OH >h^+ (Fig. S28–29). Compared with these systems, it is found that the fractions of •OH and h^+ obviously increase while the proportion of •O_2^- (the reduction of O_2) decreases, showing that the oxidation of H_2O (generating •OH) and direct pollutant oxidation (oxidation by h^+) become the dominant reactions in hm-m-WO_3/PEC with the formation of the heterophase junction. This change is directly caused by the built-in electric field at the interface of the heterophase junction, which promotes the charge separation and makes more h^+ available for the reaction. In the hm-m-WO_3/PEC system, more h^+ generated can be effectively separated and utilized for the oxidative reaction, leading to the enhanced concentration of •OH and h^+ and their contribution to BPA degradation.

Electron paramagnetic resonance (EPR) spin trapping with 5,5-dimethyl-1-pyrroline N-oxide (DMPO) in the PEC process by hm-m-WO_3 confirmed the existence of •OH and •O_2^-. Fig. 6b shows the produced •OH is captured and evidenced as the four characteristic peaks with a peak strength of 1:2:2:1 of DMPO-•OH. Besides, a strong bond signal of DMPO-•O_2^- (1:1:1:1) is detected in the PEC system in the presence of MeOH, indicating the existence of •O_2^-. No signal is observed in the blank experiment. Besides, a decrease signal of EPR-TEMPOL after PEC reaction compared with primary EPR-TEMPOL signal (Fig. 6d) also clarified that •O_2^- is involved in this system, since TEMPOL is a paramagnetic superoxide scavenger which can react with •O_2^- to form diamagnetic species [49].

The Photoluminescence (PL) emission spectra with the addition of terephthalic acid (TA) was used to detect the generation of ·OH verse reaction time [50]. A gradual enhancing of the PL intensity at 425 nm is observed as the reaction time prolonging (Fig. 6c). Moreover, the PL intensity increases linearly as a function of reaction time (Fig. S30), implying the content of produced ·OH on the surface of hm-m-WO_3 is proportional to the PEC reaction time. Importantly, the PL intensity of hm-m-WO_3 is higher than that of h-WO_3 or m-WO_3, indicating a higher formation rate of ·OH for hm-m-WO_3 during the PEC process (Fig. S28). These results confirm that the •OH with a strong oxidative ability (2.38 V_{SHE}) is generated in the hm-m-WO_3/PEC process.

UPLC-MS analysis was also employed to primarily identify the possible intermediates and fully understand the degradation process (Fig. S31–34). Based on the intermediates detected, the possible degradation pathways of BPA were proposed in Fig. 6e [51–53]. The degradation is initiated by the direct -OH addition of BPA or the β-scission of isopropyl between two phenyl groups in BPA. Afterwards, the reaction products were oxidized to low-molecular-weight intermediates and further transformed to CO_2 and H_2O.

According to the above results, the detailed degradation mechanism is proposed and exhibited in Fig. 6f. Under the light illumination, the WO_3 absorbs photons and generates electron-hole pairs which participate in the redox reaction. The built-in electric field at the interface of the hexagonal-monoclinic phase junction of WO_3 and direction of the external circuit by applying bias voltage provides the driving force for efficient charge separation. In addition, owing to the existence of the Schottky junction, the electrons can easily transfer from m-WO_3 to W mesh and the Schottky barrier increases the resistance of electron transfer from W mesh to WO_3. In such a system, more holes are utilized

for •OH generation and organics oxidation. In addition, the system contains abundant O_2 which originated from the dissolved O_2 in the electrolyte and O_2 evolution process *via* H_2O oxidation. Therefore, •O_2^- can also be generated *via* the reduction of O_2 in electrolyte by electron which transfers from the counter electrode or the W mesh directly, and the •O_2^- as oxidative species can also participate in the BPA degradation [54,55]. In the meantime, the fluid diffusion and the transfer of pollutants/ROS in the whole system are improved by the network electrode. As a result, the hm-m-WO_3/W mesh electrode shows enhanced charge separation efficiency, optimized pollutant containing fluid diffusion properties in the system, and thereby a greatly increased degradation efficiency of BPA.

3.7. Stability and economic viability analysis

Prolonging the reaction time (300 min) further degrades and mineralizes BPA (Fig. 7a), where TOC removal efficiency reaches 84.5% and TOC decreases to 2.4 ppm, which is well below the goal of maximum contamination of drinking water (4 ppm) set by US Environmental Protection Agency. Fig. 7b shows the cyclic BPA degradation tests, where the hm-m-WO_3 remains high activity (99.8% of BPA removal and 55.9% of TOC removal) at least five cycles of PEC degradation tests. The SEM of hm-m-WO_3/W mesh after 5 h′ reaction (Fig. S35) reveals the coexistence of hexagonal prisms and nanoplates, and the surface of the hexagonal prisms became rough, which is attributed to the continuous reactions at the active sites. Besides, no obvious change in hm-m-WO_3 structure is detected according to the XRD pattern after reaction (Fig. S36), and the weight of the photoelectrode before and after reaction exhibits no change (Table S3). The above results imply an excellent durability of the catalyst. Favorable stability of the photoanode is attributed to the structural stability of WO_3 in acidic conditions and the *in-situ* growing strategy of the WO_3 electrode that enhances the mechanical strength between W mesh and catalysts.

Moreover, the economic costs associated with the consumed electric energy in the hm-m-WO_3/W mesh/PEC system for removing BPA per g and TOC per g are further calculated to be US$ 0.019 and 0.052, respectively. Fig. 7c illustrates the complete processing route of wastewater to clean water, in which the PEC treatment process not only utilizes the photo energy, but also utilize the electric energy generated from Photovoltaic system, which fully highlights the sustainability and economic viability of the PEC process and demonstrates it as a promising treatment for refractory wastewater [56,57].

4. Conclusion

In summary, the network photoelectrode with a mixed WO_3 phases catalysts supported on W mesh (hm-m-WO_3/W mesh) is successfully prepared and used for PEC degradation of refectory pollutants. It shows superior PEC performance (5.6 mA cm^{-2} at 1.2 V_{RHE}) and outstanding degradation efficiency on refractory pollutant (99.9% of BPA degradation and 84.5% of TOC removal). The superior degradation performance originates from the improved charge separation efficiency and optimized mass transportation across the catalysts and in the system. In detail, the formation of Schottky junction in the W/WO_3 interface promotes charge transfer between catalysts and electrode and charge separation. And with appropriate phase alignments and interface structure in catalysts, the built-in electric field of heterophase junction provides a driven force to further improve charge separation efficiency. Therefore, the separated holes transfer onto the surface of the catalysts for generating ROS species, which takes responsibility for the degradation of pollutants. The network structure of photoelectrode optimizes the fluid diffusion and improves mass transportation of reactant/ROS in the system, which facilitates the PEC degradation process. This work demonstrates an approach for designing an efficient photoelectrocatalyst in degradation and mineralization of organic pollutants, and provides in-depth understanding of charge separation and mass transportation in
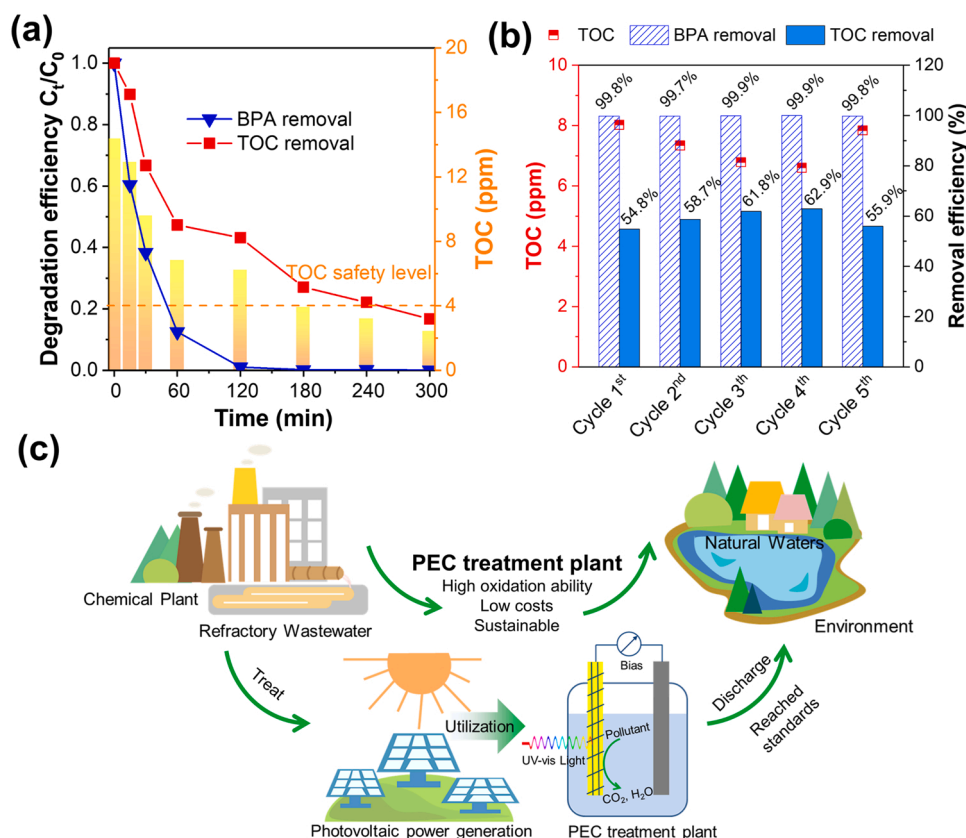
Fig. 7. (a) PEC degradation of BPA with reaction time prolonged. (b) Cyclic PEC degradation. (c) Schematic representation of PEC treatment process in a sustainable way.

PEC system.

CRediT authorship contribution statement

Qiuling Ma: Conceptualization; Methodology; Writing – original draft; Writing – review & editing; Formal analysis; **Rui song:** Methodology; Investigation; **Fujun Ren:** Investigation; **Hao Wang:** Investigation; **Wensheng Gao:** Conceptualization; **Zelong Li:** Writing – original draft; Writing – review & editing; Supervision; **Can Li:** Writing – review & editing; Supervision; Project administration; Funding acquisition.

Declaration of Competing Interest

The authors declare that they have no known competing financial interests or personal relationships that could have appeared to influence the work reported in this paper.

Appendix A. Supporting information

Supplementary data associated with this article can be found in the online version at doi:10.1016/j.apcatb.2022.121292.

References

[1] M.F. Meyer, S.M. Powers, S.E. Hampton, An evidence synthesis of pharmaceuticals and personal care products (PPCPs) in the environment: imbalances among compounds, sewage treatment techniques, and ecosystem types, Environ. Sci. Technol. 53 (2019) 12961–12973, https://doi.org/10.1021/acs.est.9b02966.

[2] M. Patel, R. Kumar, K. Kishor, T. Mlsna, C.U. Pittman, D. Mohan, Pharmaceuticals of emerging concern in aquatic systems: chemistry, occurrence, effects, and removal methods, Chem. Rev. 119 (2019) 3510–3673, https://doi.org/10.1021/acs.chemrev.8b00299.

[3] J. Woodward, J. Li, J. Rothwell, R. Hurley, Acute riverine microplastic contamination due to avoidable releases of untreated wastewater, Nat. Sustain. 4 (2021) 793–802, https://doi.org/10.1038/s41893-021-00718-2.

[4] H. Kim, K. Shim, K.E. Lee, J.W. Han, Y. Zhu, W. Choi, Photocatalytic production of H_2O_2 from water and dioxygen only under visible light using organic polymers: Systematic study of the effects of heteroatoms, Appl. Catal. B Environ. 299 (2021), 120666, https://doi.org/10.1016/j.apcatb.2021.120666.

[5] M. Ling, H. Shang, H. Li, Y. Hong, C. Ling, K. Wei, B. Zhou, C. Mao, Z. Ai, L. Zhang, Kirkendall, Effect boosts phosphorylated nZVI for efficient heavy metal wastewater treatment, Angew. Chem. Int. Ed. 60 (2021) 17115–17122, https://doi.org/10.1002/anie.202104586.

[6] J. Xu, X. Zheng, Z. Feng, Z. Lu, Z. Zhang, W. Huang, Y. Li, D. Vuckovic, Y. Li, S. Dai, G. Chen, K. Wang, H. Wang, J.K. Chen, W. Mitch, Y. Cui, Organic wastewater treatment by a single-atom catalyst and electrolytically produced H_2O_2, Nat. Sustain. 4 (2021) 233–241, https://doi.org/10.1038/s41893-020-00635-w.

[7] M. Sun, R.-T. Gao, J. He, X. Liu, T. Nakajima, X. Zhang, L. Wang, Photo-driven oxygen vacancies extends charge carrier lifetime for efficient solar water splitting, Angew. Chem. Int. Ed. 60 (2021) 17601–17607, https://doi.org/10.1002/anie.202104754.

[8] Y. Guo, X. Quan, N. Lu, H. Zhao, S. Chen, High photocatalytic capability of self-assembled nanoporous WO_3 with preferential orientation of (002) planes, Environ. Sci. Technol. 41 (2007) 4422–4427, https://doi.org/10.1021/es062546c.

[9] J. Ma, K. Mao, J. Low, Z. Wang, D. Xi, W. Zhang, H. Ju, Z. Qi, R. Long, X. Wu, L. Song, Y. Xiong, Efficient photoelectrochemical conversion of methane into ethylene glycol by WO_3 nanobar arrays, Angew. Chem. Int. Ed. 60 (2021) 9357–9361, https://doi.org/10.1002/anie.202101701.

[10] Z. Wei, F. Liang, Y. Liu, W. Luo, J. Wang, W. Yao, Y. Zhu, Photoelectrocatalytic degradation of phenol-containing wastewater by TiO_2/g-C_3N_4 hybrid heterostructure thin film, Appl. Catal. B Environ. 201 (2017) 600–606, https://doi.org/10.1016/j.apcatb.2016.09.003.

[11] Q. Niu, X. Gu, L. Li, Y.-n Zhang, G. Zhao, 3D CQDs-{001}TiO₂/Ti photoelectrode with dominant {001} facets: efficient visible-light-driven photoelectrocatalytic oxidation of organic pollutants and mechanism insight, Appl. Catal. B Environ. 261 (2020), 118229, https://doi.org/10.1016/j.apcatb.2019.118229.

[12] L. Li, Z. Hu, J.C. Yu, On-demand synthesis of H₂O₂ by water oxidation for sustainable resource production and organic pollutant degradation, Angew. Chem. Int. Ed. 59 (2020) 20538–20544, https://doi.org/10.1002/anie.202008031.

[13] M. Wang, L. Sun, Z. Lin, J. Cai, K. Xie, C. Lin, p–n Heterojunction photoelectrodes composed of Cu₂O-loaded TiO₂ nanotube arrays with enhanced photoelectrochemical and photoelectrocatalytic activities, Energy Environ. Sci. 6 (2013) 1211–1220, https://doi.org/10.1039/C3EE24162A.

[14] Y. Hou, X. Li, Q. Zhao, X. Quan, G. Chen, Electrochemically assisted photocatalytic degradation of 4-Chlorophenol by ZnFe₂O₄−Modified TiO₂ nanotube array electrode under visible light irradiation, Environ. Sci. Technol. 44 (2010) 5098–5103, https://doi.org/10.1021/es100004u.

[15] J. Qu, X. Zhao, Design of BDD-TiO₂ hybrid electrode with P−N function for photoelectrocatalytic degradation of organic contaminants, Environ. Sci. Technol. 42 (2008) 4934–4939, https://doi.org/10.1021/es702769p.

[16] C. Hu, S. Tu, N. Tian, T. Ma, Y. Zhang, H. Huang, Photocatalysis enhanced by external fields, Angew. Chem. Int. Ed. 60 (2021) 16309–16328, https://doi.org/10.1002/anie.202009518.

[17] D. Pan, S. Xiao, X. Chen, R. Li, Y. Cao, D. Zhang, S. Pu, Z. Li, G. Li, H. Li, Efficient photocatalytic fuel cell via simultaneous visible-photoelectrocatalytic degradation and electricity generation on a porous coral-like WO₃/W photoelectrode, Environ. Sci. Technol. 53 (2019) 3697–3706, https://doi.org/10.1021/acs.est.8b05685.

[18] M.S. Koo, X. Chen, K. Cho, T. An, W. Choi, In Situ Photoelectrochemical chloride activation using a WO₃ electrode for oxidative treatment with simultaneous H₂ evolution under visible light, Environ. Sci. Technol. 53 (2019) 9926–9936, https://doi.org/10.1021/acs.est.9b02401.

[19] Y. Liu, L. Liang, C. Xiao, X. Hua, Z. Li, B. Pan, Y. Xie, Promoting photogenerated holes utilization in pore-rich WO₃ ultrathin nanosheets for efficient xxygen-evolving photoanode, Adv. Energy Mater. 6 (2016) 1600437, https://doi.org/10.1002/aenm.201600437.

[20] G.L. Chiarello, M. Bernareggi, M. Pedroni, M. Magni, S.M. Pietralunga, A. Tagliaferri, E. Vassallo, E. Selli, Enhanced photopromoted electron transfer over a bilayer WO₃ n-n heterojunction prepared by RF diode sputtering, J. Mater. Chem. A 5 (2017) 12977–12989, https://doi.org/10.1039/C7TA03887A.

[21] J.H. Baek, B.J. Kim, G.S. Han, S.W. Hwang, D.R. Kim, I.S. Cho, H.S. Jung, BiVO₄/WO₃/SnO₂ double-heterojunction photoanode with enhanced charge separation and visible-transparency for bias-free solar water-splitting with a perovskite solar cell, ACS Appl. Mater. Interfaces 9 (2017) 1479–1487, https://doi.org/10.1021/acsami.6b12782.

[22] P.M. Rao, L. Cai, C. Liu, I.S. Cho, C.H. Lee, J.M. Weisse, P. Yang, X. Zheng, Simultaneously efficient light absorption and charge separation in WO₃/BiVO₄ core/shell nanowire photoanode for photoelectrochemical water oxidation, Nano Lett. 14 (2014) 1099–1105, https://doi.org/10.1021/nl500022z.

[23] Q. Zeng, J. Li, L. Li, J. Bai, L. Xia, B. Zhou, Synthesis of WO₃/BiVO₄ photoanode using a reaction of bismuth nitrate with peroxovanadate on WO₃ film for efficient photoelectrocatalytic water splitting and organic pollutant degradation, Appl. Catal. B Environ. 217 (2017) 21–29, https://doi.org/10.1016/j.apcatb.2017.05.072.

[24] M. Ma, K. Zhang, P. Li, M.S. Jung, M.J. Jeong, J.H. Park, Dual oxygen and tungsten vacancies on a WO₃ photoanode for enhanced water oxidation, Angew. Chem. Int. Ed. 55 (2016) 11819–11823, https://doi.org/10.1002/anie.201605247.

[25] Z. Wei, W. Wang, W. Li, X. Bai, J. Zhao, E.C.M. Tse, D.L. Phillips, Y. Zhu, Steering electron–hole migration pathways using oxygen vacancies in tungsten oxides to enhance their photocatalytic oxygen evolution performance, Angew. Chem. Int. Ed. 60 (2021) 8236–8242, https://doi.org/10.1002/anie.202016170.

[26] X. Ning, P. Du, Z. Han, J. Chen, X. Lu, Insight into the transition-metal hydroxide cover layer for enhancing photoelectrochemical water oxidation, Angew. Chem. Int. Ed. 60 (2021) 3504–3509, https://doi.org/10.1002/anie.202013014.

[27] Y. Li, Q. Mei, Z. Liu, X. Hu, Z. Zhou, J. Huang, B. Bai, H. Liu, F. Ding, Q. Wang, Fluorine-doped iron oxyhydroxide cocatalyst: promotion on the WO₃ photoanode conducted photoelectrochemical water splitting, Appl. Catal. B Environ. 304 (2022), 120995, https://doi.org/10.1016/j.apcatb.2021.120995.

[28] A. Li, Z. Wang, H. Yin, S. Wang, P. Yan, B. Huang, X. Wang, R. Li, X. Zong, H. Han, C. Li, Understanding the anatase–rutile phase junction in charge separation and transfer in a TiO₂ electrode for photoelectrochemical water splitting, Chem. Sci. 7 (2016) 6076–6082, https://doi.org/10.1039/C6SC01611A.

[29] X. Wang, S. Jin, H. An, X. Wang, Z. Feng, C. Li, Relation between the photocatalytic and photoelectrocatalytic performance for the particulate semiconductor-based photoconversion systems with surface phase junction structure, J. Phys. Chem. C. 119 (2015) 22460–22464, https://doi.org/10.1021/acs.jpcc.5b06347.

[30] X. Wang, C. Li, Roles of phase junction in photocatalysis and photoelectrocatalysis, J. Phys. Chem. C. 122 (2018) 21083–21096, https://doi.org/10.1021/acs.jpcc.8b06039.

[31] Y. Lu, J. Zhang, F. Wang, X. Chen, Z. Feng, C. Li, K₂SO₄-assisted hexagonal/monoclinic WO₃ phase junction for efficient photocatalytic degradation of RhB, ACS Appl. Energy Mater. 1 (2018) 2067–2077, https://doi.org/10.1021/acsaem.8b00168.

[32] M. Kang, J. Liang, F. Wang, X. Chen, Y. Lu, J. Zhang, Structural design of hexagonal/monoclinic WO₃ phase junction for photocatalytic degradation, Mater. Res. Bull. 121 (2020), 110614, https://doi.org/10.1016/j.materresbull.2019.110614.

[33] T. Wei, Y.-N. Zhu, Z. Gu, X. An, L.-m Liu, Y. Wu, H. Liu, J. Tang, J. Qu, Multi-electric field modulation for photocatalytic oxygen evolution: Enhanced charge

[34] Z. Gu, X. An, H. Lan, Y. Tian, J. Zhang, R. Liu, H. Liu, J. Qu, Microfluidic-enhanced 3-D photoanodes with free interfacial energy barrier for photoelectrochemical applications, Appl. Catal. B Environ. 244 (2019) 740–747, https://doi.org/10.1016/j.apcatb.2018.12.009.

[35] S.S. Kalanur, Y.J. Hwang, S.Y. Chae, O.S. Joo, Facile growth of aligned WO₃ nanorods on FTO substrate for enhanced photoanodic water oxidation activity, J. Mater. Chem. A 1 (2013) 3479–3488, https://doi.org/10.1039/C3TA01175E.

[36] X. Feng, Y. Chen, Z. Qin, M. Wang, L. Guo, Facile fabrication of sandwich structured WO₃ nanoplate arrays for efficient photoelectrochemical water splitting, ACS Appl. Mater. Interfaces 8 (2016) 18089–18096, https://doi.org/10.1021/acsami.6b04887.

[37] L. Liu, Y. Zhang, H. Huang, Junction engineering for photocatalytic and photoelectrocatalytic CO₂ reduction, Sol. RRL 5 (2020), 2000430, https://doi.org/10.1002/solr.202000430.

[38] S. Chen, S. Wang, C. Wang, Z. Wang, Q. Liu, Latest advance on seamless metal-semiconductor contact with ultralow Schottky barrier in 2D-material-based devices, Nanotaday 42 (2022), 101372, https://doi.org/10.1016/j.nantod.2021.101372.

[39] Z. Zhao, L. Zheng, W. Hu, H. Zheng, Synergistic effect of silane and graphene oxide for enhancing the photoelectrochemical water oxidation performance of WO₃ NS arrays, Electrochim. Acta 292 (2018) 322–330, https://doi.org/10.1016/j.electacta.2018.09.164.

[40] Y. Wang, W. Tian, C. Chen, W. Xu, L. Li, Tungsten trioxide nanostructures for photoelectrochemical water splitting: material engineering and charge carrier dynamic manipulation, Adv. Funct. Mater. 29 (2019), 1809036, https://doi.org/10.1002/adfm.201809036.

[41] F. Chen, H. Huang, L. Guo, Y. Zhang, T. Ma, The role of polarization in photocatalysis, Angew. Chem. Int. Ed. 58 (2019) 10061–10073, https://doi.org/10.1002/anie.201901361.

[42] R. Li, H. Han, F. Zhang, D. Wang, C. Li, Highly efficient photocatalysts constructed by rational assembly of dual-cocatalysts separately on different facets of BiVO₄, Energy Environ. Sci. 7 (2014) 1369–1376, https://doi.org/10.1039/C3EE43304H.

[43] G. Liu, J. Shi, F. Zhang, Z. Chen, J. Han, C. Ding, S. Chen, Z. Wang, H. Han, C. Li, A Tantalum nitride photoanode modified with a hole-storage layer for highly stable solar water splitting, Angew. Chem. Int. Ed. 53 (2014) 7295–7299, https://doi.org/10.1002/anie.201404697.

[44] J. Zhang, X. Chang, C. Li, A. Li, S. Liu, T. Wang, J. Gong, WO₃ photoanodes with controllable bulk and surface oxygen vacancies for photoelectrochemical water oxidation, J. Mater. Chem. A 6 (2018) 3350–3354, https://doi.org/10.1039/C7TA10056F.

[45] Z. Wang, X. Zong, Y. Gao, J. Han, Z. Xu, Z. Li, C. Ding, S. Wang, C. Li, Promoting charge separation and injection by optimizing the interfaces of GaN:ZnO photoanode for efficient solar water oxidation, ACS Appl. Mater. Interfaces 9 (2017) 30696–30702, https://doi.org/10.1021/acsami.7b09021.

[46] L. Liu, W. Cai, Y. Chen, Y. Wang, Fluid dynamics and mass transfer Study of electrochemical oxidation by CFD prediction and experimental validation, Ind. Eng. Chem. Res. 57 (2018) 6493–6504, https://doi.org/10.1021/acs.iecr.7b04226.

[47] S. Weon, E. Choi, H. Kim, J.Y. Kim, H.-J. Park, S.-m Kim, W. Kim, W. Choi, Active {001} facet exposed TiO₂ nanotubes photocatalyst filter for volatile organic compounds removal: from material development to commercial indoor air cleaner application, Environ. Sci. Technol. 52 (2018) 9330–9340, https://doi.org/10.1021/acs.est.8b02282.

[48] J. Wang, S. Wang, Reactive species in advanced oxidation processes: formation, identification and reaction mechanism, Chem. Eng. J. 401 (2020), 126158, https://doi.org/10.1016/j.cej.2020.126158.

[49] S. Scheinok, P. Leveque, P. Sonveaux, B. Driesschaert, B. Gallez, Comparison of different methods for measuring the superoxide radical by EPR spectroscopy in buffer, cell lysates and cells, Free Radic. Res. 52 (2018) 1182–1196, https://doi.org/10.1080/10715762.2018.1541321.

[50] D. Jassby, J. Farner Budarz, M. Wiesner, Impact of aggregate size and structure on the photocatalytic properties of TiO₂ and ZnO nanoparticles, Environ. Sci. Technol. 46 (2012) 6934–6941, https://doi.org/10.1021/es2009099h.

[51] C. Guo, M. Ge, L. Liu, G. Gao, Y. Feng, Y. Wang, Directed synthesis of mesoporous TiO₂ microspheres: catalysts and their photocatalysis for bisphenol A degradation, Environ. Sci. Technol. 44 (2010) 419–425, https://doi.org/10.1021/es9019854.

[52] R.S. Sahu, Y.-h Shih, W.-L. Chen, New insights of metal free 2D graphitic carbon nitride for photocatalytic degradation of bisphenol A, J. Hazard. Mater. 402 (2021), 123509, https://doi.org/10.1016/j.jhazmat.2020.123509.

[53] S. Wang, J. Tian, Q. Wang, F. Xiao, S. Gao, W. Shi, F. Cui, Development of CuO coated ceramic hollow fiber membrane for peroxymonosulfate activation: a highly efficient singlet oxygen-dominated oxidation process for bisphenol a degradation, Appl. Catal. B Environ. 256 (2019), 117783, https://doi.org/10.1016/j.apcatb.2019.117783.

[54] M.S. Koo, K. Cho, J. Yoon, W. Choi, Photoelectrochemical degradation of organic compounds coupled with molecular hydrogen generation using electrochromic TiO₂ nanotube arrays, Environ. Sci. Technol. 51 (2017) 6590–6598, https://doi.org/10.1021/acs.est.7b00774.

[55] S. Xie, C. Tang, H. Shi, G. Zhao, Highly efficient photoelectrochemical removal of atrazine and the mechanism investigation: bias potential effect and reactive

species, J. Hazard. Mater. 415 (2021), 125681, https://doi.org/10.1016/j.jhazmat.2021.125681.

[56] J. Zhang, G. Zhang, H. Lan, J. Qu, H. Liu, Synergetic hydroxyl radical oxidation with atomic hydrogen reduction lowers the organochlorine conversion barrier and potentiates effective contaminant mineralization, Environ. Sci. Technol. 55 (2021) 3296–3304, https://doi.org/10.1021/acs.est.0c07271.

[57] R.R. Hernandez, A. Armstrong, J. Burney, G. Ryan, K. Moore-O'Leary, I. Diédhiou, S.M. Grodsky, L. Saul-Gershenz, R. Davis, J. Macknick, D. Mulvaney, G.A. Heath, S. B. Easter, M.K. Hoffacker, M.F. Allen, D.M. Kammen, Techno–ecological synergies of solar energy for global sustainability, Nat. Sustain. 2 (2019) 560–568, https://doi.org/10.1038/s41893-019-0309-z.